Journal of Alloys and Compounds 1048 (2025) 185048

Contents lists available at ScienceDirect

Journal of Alloys and Compounds

journal homepage: www.elsevier.com/locate/jalcom

Exploring a route to induce ferromagnetism on $Sr_3Sn_2O_7$ by co-doping with non-Jahn-Teller-distorted Mn^{3+} and La^{3+} cations

J. Blasco [a,b,*], V. Cuartero [a,c], S. Lafuerza [a,b], D. Gracia [a,b], I. Puente-Orench [d], J.A. Rodríguez-Velamazán [d], J. Herrero-Martín [e], R. Torchio [f], O. Mathon [f], G. Subías [a,b]

[a] Instituto de Nanociencia y Materiales de Aragón (INMA), CSIC-Universidad de Zaragoza, Zaragoza 50009, Spain
[b] Departamento de Física de la Materia Condensada, Universidad de Zaragoza, C/ Pedro Cerbuna 12, Zaragoza 50009, Spain
[c] Departamento de Ciencia y Tecnología de Materiales y Fluidos, EINA, Universidad de Zaragoza, C/María de Luna 3, Zaragoza 50018, Spain
[d] Institut Laue-Langevin, Boîte Postale 156, Grenoble 38042, France
[e] CELLS-ALBA Synchrotron, Barcelona 08290, Spain
[f] ESRF – The European Synchrotron Radiation Facility, 71 Avenue des Martyrs, Grenoble 38000, France

ARTICLE INFO

Keywords:
Multiferroics
Improper ferroelectricity
Cluster-glass
EXAFS
Phase transition

ABSTRACT

We here explore a route to induce a ferromagnetic ground state on the Ruddlesden-Popper phases $Sr_{3-x}La_xSn_{2-x}Mn_xO_7$ replacing Sn by Mn up to $x = 1.25$. Samples with low Mn concentration ($x \leq 0.1$) adopt the polar $A2_1am$ space group, consistent with previously reported ferroelectric behavior. For higher Mn concentrations ($x \geq 0.25$) the samples adopt the centrosymmetric space group *Amam* due to the suppression of specific rotational modes. X-ray absorption spectroscopy confirmed the presence of a Mn^{3+} ion in all samples though it is not Jahn-Teller distorted. An undistorted MnO_6 octahedral local structure is reported instead, with Debye-Waller factors for the Mn-O bond length increasing as Mn content does, due to the disorder induced in the Sn/Mn sublattice and the rising of rumpling distortions (expansion of the perovskite bilayer coupled with shrinkage of the rock salt layer). All the $Sr_{3-x}La_xSn_{2-x}Mn_xO_7$ samples exhibit ferromagnetic correlations. While Mn^{3+} cations in low Mn-content samples ($x \leq 0.25$) agree with spin-only contributions, higher doping levels deviate from this interpretation, possibly due to the enhancement of magnetic interactions. At 5 K, all samples exhibit spontaneous magnetization which increases with Mn content, but the Mn^{3+} magnetic sublattice is not fully polarized. Neutron diffraction confirmed the absence of long-range magnetic order and AC susceptibility analysis indicates a cluster-glass magnetic state due to structural disorder and competing interactions. Compared to simple perovskites, our results indicate that the rock salt layer plays a key role in suppressing long-range ferromagnetic order, making it particularly challenging to achieve multiferroic behavior by doping hybrid improper ferroelectrics with magnetic cations.

1. Introduction

In recent times there has been great interest in the study of magnetoelectric multiferroic materials [1,2]. A magnetoelectric multiferroic material (hereafter denoted as multiferroic) exhibits simultaneous (anti) ferromagnetic and ferroelectric orderings within a single phase, making it very promising for applications in sensors, actuators, or new types of electronic memory devices [3]. However, multiferroic materials are very scarce because (anti)ferromagnetic and ferroelectric orderings tend to have exclusive chemical and structural requirements. Ferroelectricity generally arises from the presence of non-magnetic d^0 cations (like Ti^{4+} in $BaTiO_3$), while ferromagnetism typically requires partially filled *d* or *f* orbitals. Combining both requirements in a single material is challenging because the same electronic configuration that promotes one property can inhibit the other [4]. In addition, the mechanisms that stabilize ferromagnetism (e.g., exchange interaction) and ferroelectricity (e.g., ion displacement) can be mutually exclusive, making it difficult to achieve and maintain both properties in a single material [5]. Consequently, a great effort has been made in the search for mechanisms that can favor both types of orderings, like, for instance, the hybrid improper ferroelectric (HIF) mechanism, which is active in layered structures like Ruddlesden-Popper (RP) or Aurivillius phases [6,7]. This

* Corresponding author at: Instituto de Nanociencia y Materiales de Aragón (INMA), CSIC-Universidad de Zaragoza, Zaragoza 50009, Spain.
E-mail address: jbc@unizar.es (J. Blasco).

https://doi.org/10.1016/j.jallcom.2025.185048
Received 14 July 2025; Received in revised form 23 September 2025; Accepted 13 November 2025
Available online 17 November 2025

mechanism involves the combination of two non-polar structural distortions (rotation and tilts of oxygen octahedra) that when combined in a layered structure, favor the condensation of a secondary polar distortion, breaking the center symmetry and favoring a polar structure [8,9]. This mechanism is fully functional with magnetic cations so it is possible to finely tune the electrical and magnetic properties of these materials through chemical substitutions [10].

Recently, the HIF mechanism has been proved in $Sr_3Sn_2O_7$ with switchable electric polarization at room temperature [11,12] and with a ferroelectric transition temperature of T_{FE}= 410 K [13]. This compound belongs to the family of double-layer RP phases (with general formula $A_3B_2O_7$) and the structure consists of two layers of perovskite with corner-sharing SnO_6 octahedra separated by a rock-salt layer of SrO along the *c*-axis [14]. The substitution of Sr^{2+} with other divalent cations affects the magnitude of the oxygen octahedra tilts and rotations, and consequently T_{FE}. When Sr^{2+} is replaced by Ba^{2+}, T_{FE} decreases [15], while the opposite effect is observed for Ca^{2+} substitution [16]. These results led these authors to propose a relationship between T_{FE} and the Goldschmidt tolerance factor (*t*-factor) of perovskites [17], and therefore, it makes feasible to design chemical substitutions that optimize the *t*-values to give rise the appropriate tilts and rotations of the BO_6 octahedra [10]. Following this strategy, some of us managed to introduce magnetic atoms into the $Sr_3Sn_2O_7$ network using a co-doping strategy [18]. A trivalent magnetic cation is introduced at the Sn site as Sr is replaced by La, to preserve the electrical balance. Single phases were obtained but a decrease in T_{FE} was observed, which indicates that T_{FE} does not only depend on the *t*-value and further effects, such as rumpling distortions [19] or structural disorder, should be considered [18]. Furthermore, achieving a multiferroic material requires incorporating a sufficient concentration of magnetic atoms into the lattice to overcome the magnetic percolation threshold. Recent efforts made with Fe and Cr, that present strong antiferromagnetic couplings, have shown that achieving such percolation is difficult in this type of crystal structure [20].

We here explore a route to induce a ferromagnetic ground state on the $Sr_{3-x}La_xSn_{2-x}Mn_xO_7$ series by substituting Sn^{4+} by Mn^{3+} up to $x \geq 1.25$, which exceeds the 50 % magnetic cations threshold achieved in this system through other types of substitutions [20]. Mn^{3+}cation paves the way for studying different types of magnetic interactions. Mn^{3+} has a $3d^4$ ($t_{2g}^3e_g^1$) electronic configuration, able to exhibit a strong Jahn-Teller (JT) effect [21]. Cooperative JT distortions of the MnO_6 octahedra may be accommodated as a checkerboard pattern where the e_g orbitals of adjacent Mn^{3+} ions are oppositely oriented [22]. This leads to anisotropic magnetic interactions like the ones observed in the A-type magnetic ordering of stoichiometric $LaMnO_3$ [23]. Otherwise, when Mn^{3+} cations are diluted in a non-magnetic matrix like the simple $LaGa_{1-x}Mn_xO_3$ or $LaSc_{1-x}Mn_xO_3$ [24,25] perovskites, a ferromagnetic ground state is stabilized for compositions around $x = 0.5$ [26] explained in terms of a vibronic superexchange mechanism [25]. Sn^{4+} is a cation with a fully filled *4d* band, similar to Ga^{3+}, which has a completed *3d* band. In addition, a ferromagnetic ground state has been reported for the simple perovskite $La_{1/2}Sr_{1/2}Mn_{1/2}Sn_{1/2}O_3$ [27] suggesting that the vibronic mechanism is also operative in this system.

2. Experimental details

Polycrystalline samples of $Sr_{3-x}La_xSn_{2-x}Mn_xO_7$ ($0 \leq x \leq 1.25$) were synthesized by solid state reaction. Stoichiometric amounts of SnO_2, $SrCO_3$, La_2O_3 and Mn_2O_3 were mixed, ground and heated at 1000º C for 15 h in air. The resulting powder was reground, pressed into pellets and sintered at 1300º C for 24 h. Then, the pellets were reground, repressed and sintered at 1400º C for another 24 h under Ar atmosphere. The heating and cooling ramps were 5ºC/min in all steps. For the sake of comparison, a sample of $La_{1/2}Sr_{1/2}Sn_{1/2}Mn_{1/2}O_3$ was prepared following the synthesis reported in ref. 27. The samples were characterized by X-ray powder diffraction (XRD) using a Rigaku D-system using Cu $K\alpha_{1,2}$ wavelengths and an angular range of $6º \leq 2\theta \leq 135º$ at room temperature. Neutron powder diffraction (NPD) measurements were performed at the high-flux reactor of the ILL (Grenoble, France) using the high-intensity powder diffractometer D1B with a detector angular range coverage $5º \leq 2\theta \leq 128º$, which is especially suited for magnetic structure determination. A wavelength of $\lambda \approx 2.52$ Å was used in a temperature range between 2 K and 150 K. Rietveld analyses of both XRD and NPD patterns were performed with the Fullprof program [28]. The chemical composition of the samples was tested by using the wavelength dispersive X-ray fluorescence spectrometry technique (advant'XP+ model manufactured by ARL). The Sr:La:Sn:Mn ratio agreed with the nominal one for all samples.

Magnetic measurements were carried out between 5 and 400 K using a commercial superconducting quantum interference device (SQUID) magnetometer from Quantum Design. The measurements were performed warming the sample after zero-field cooling at an external magnetic field of 1 kOe. Isothermal magnetization measurements at selected temperatures between 5 and 250 K were performed for external fields between −50 and 50 kOe.

Mn-$L_{2,3}$ (630 −670 eV) edge X-ray absorption spectroscopy (XAS) measurements were performed at the HECTOR cryomagnet end station in the BL29 BOREAS beamline [29] of the ALBA synchrotron radiation facility (Barcelona, Spain). The photon flux was about 10^{12} ph/s with an energy resolution of ~50 meV. Sintered pellets were used for the XAS measurements, which were also cleaved in situ under ultrahigh vacuum conditions (~10^{-9} mbar) to obtain clean sample surfaces. Measurements were recorded in total electron yield mode (*i.e.* drain current detection) at 300 K.

Mn K-edge XAS measurements at room temperature were performed at the BM23 beamline [30] at the ESRF (Grenoble, France). The spectra were collected in fluorescence mode geometry using a multi-element silicon drift detector. A Mn foil was measured for energy calibration. The extended X-ray absorption fine structure (EXAFS) data processing and analysis were performed using Demeter software [31]. All X-ray absorption near-edge structure (XANES) signals shown here have been normalized to unity at high energy, about 40 eV above the absorption edge, after subtracting the pre-edge line.

3. Results and discussion

3.1. Room temperature crystal structure of $Sr_{3-x}La_xSn_{1-x}Mn_xO_7$ series

XRD patterns agree with a single $A_3B_2O_7$ phase for $Sr_{3-x}La_xSn_{2-x}Mn_xO_7$ samples with $x \leq 1$ (see supplementary information). For $x = 1.25$, peaks from a minor impurity of a simple perovskite, ABO_3, identified as $La_{1/2}Sr_{1/2}Sn_{1/2}Mn_{1/2}O_3$ are noticeable in the pattern. Above this value, the XRD pattern refinements reveal up to three types of phases identified as: ABO_3, A_2BO_4 and $A_3B_2O_7$. This suggests that at high Mn concentrations, the bilayer RP phase becomes unstable compared to the mixture of a simple perovskite and a single-layer RP phase. In other words, the reaction $A_3B_2O_7 \leftrightarrows ABO_3 + A_2BO_4$ is shifted to the right side as previously observed in related co-doped compounds [20]. $Sr_3Sn_2O_7$ exhibits a first-order ferroelectric-paraelectric transition at T_{FE}= 410 K and adopts a polar structure (space group No. 36, $A2_1am$) at room temperature [13,18,32]. A smooth transition is also observed in the $Sr_{2.9}La_{0.1}Sn_{1.9}Mn_{0.1}O_7$ sample at T_{FE}= 348 K [18] indicating that this sample is also ferroelectric at room temperature and therefore has the same crystallographic polar structure as the undoped sample. For the rest of the $Sr_{3-x}La_xSn_{2-x}Mn_xO_7$ samples ($x \geq 0.25$), no anomalies were observed in the dielectric permittivity measurements above room temperature, indicating that they are paraelectric at room temperature as observed in related substitutions [20].

The symmetry-adapted distortion modes were used to determine and compare distorted structures derived from the higher-symmetry tetragonal phase (space group *I4/mmm*) of $A_3B_2O_7$ RP compounds [33,34]. Fig. 1 shows the group−subgroup relationships between space

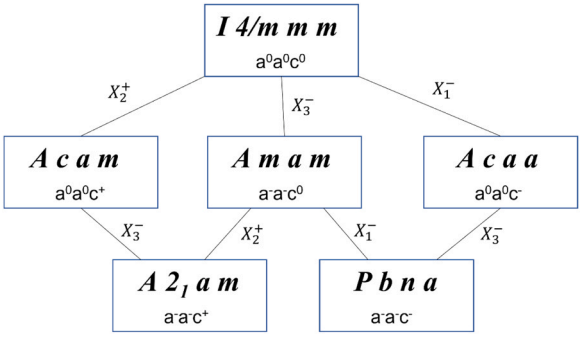

Fig. 1. Group-subgroup relationships between space groups related to the BO_6 octahedra tilts associated to the Irreps X_2^+ (in-phase rotation along *c*-axis), X_1^- (antiphase rotation along *c*-axis) and X_3^- (antiphase tilts around [1 1 0] direction) of space group *I4/mmm*. The $A2_1am$ and *Pbna* symmetries are established by the direct sums $X_2^+ \oplus X_3^-$ and $X_1^- \oplus X_3^-$, respectively. The sequences following group-subgroup relationships are allowed to be second order. The *Pbna*-to-$A2_1am$ ferroelectric phase transition, without group–subgroup relationship, cannot be continuous. The Glazer's tilt schema is indicated for each space group.

groups associated with the usual tilts and rotations of BO_6 octahedra and the corresponding tilt system following the Glazer's notation [35].

The diffraction patterns of the doped $Sr_{3-x}La_xSn_{2-x}Mn_xO_7$ samples show broad peaks whose width increases with Mn content, which prevents the unambiguous identification of the crystallographic space group. The first hypothesis is that the whole $Sr_{3-x}La_xSn_{2-x}Mn_xO_7$ series adopts the space group *Pbna* of the paraelectric phase of $Sr_3Sn_2O_7$, assuming that T_{FE} simply decreases with increasing the Mn content at the Sn site. However, the patterns of the $Sr_{3-x}La_xSn_{2-x}Mn_xO_7$ series do not show any new reflections that contradict the extinction rules of an A-centered lattice. For instance, the (1 2 3) reflection identified for the paraelectric phase of $Sr_3Sn_2O_7$ has zero intensity in our experimental patterns. Even though *Pbna* space group produced acceptable fits, the refinements yield negligible amplitudes for the modes associated with anti-phase rotations, belonging to the irreducible representation (Irrep) X_1^-. In particular, the (2 1 2) reflection, whose intensity is strongly enhanced by these anti-phase rotations, is missing in our XRD patterns which definitely excludes the *Pbna* space group for $x \geq 0.25$ samples.

Another possibility is that the Mn substitution at the Sn site forces the in-phase rotation (associated with the X_2^+ Irrep) or the antiphase tilt (X_3^- Irrep) to disappear (see Fig. S1 in supplementary information). In that case, the space groups for the paraelectric phase would be *Acam* or *Amam,* respectively (see Fig. 1). The refinements performed using the *Acam* group cannot account for some diffraction peaks arising from the antiphase tilts. In contrast, the fits using the *Amam* group could accurately explain all the diffraction peaks in the experimental XRD patterns. Good refinements can also be obtained using the ferroelectric $A2_1am$ space group, but in this case, the results show null amplitudes for X_2^+, indicating that *Amam* is the best matching space group for the paraelectric phase of $Sr_{3-x}La_xSn_{2-x}Mn_xO_7$ with $x \geq 0.25$. The refined patterns for $x = 0$ and $x = 0.1$ were reported elsewhere [18] and can be seen in the supplementary information for $x \geq 0.25$ (Fig. S2-S6). The refined structural parameters for the whole series are detailed in the supplementary material (see Tables S1 and S2). Fig. 2 shows the evolution of lattice parameters along the $Sr_{3-x}La_xSn_{2-x}Mn_xO_7$ series. The volume of the unit cell decreases linearly as the Mn content increases along the series. This must be ascribed to the different tabulated ionic radii [36] since $r^{3+}_{La} < r^{2+}_{Sr}$ and $r^{3+}_{Mn} < r^{4+}_{Sn}$ with r^{3+}_{La}, r^{2+}_{Sr}, r^{3+}_{Mn} and r^{4+}_{Sn} being the ionic radii of La^{3+}, Sr^{2+}, Mn^{3+} and Sn^{4+}, respectively. However, while the *a* and *b* axes show a continuous decrease throughout the series, the shrinkage of the *c* axis seems to reach its limit for $x = 1$, the last single-phase sample.

Refined bond lengths for $Sn(Mn)O_6$ octahedron are reported in the supplementary information for the whole series (see Table S3). Valences obtained from the bond valence sums (BVS) method [37] agree with a Sn^{4+} cation in the $Sr_3Sn_2O_7$ lattice. For low Mn concentrations, BVS indicates that Mn is nearly 3+ but slightly underbonded as it occupies more space in the solid solution than expected, likely due to the larger ionic radius of Sn^{4+}. As the Mn content increases, this atom becomes progressively less underbonded, whereas Sn^{4+} ions tend to become overbonded as a result of the unit cell contraction (see Table S3). For $x \geq 0.25$, Sn(Mn) have an octahedral coordination with five similar Sn (Mn)-O distances and a more elongated sixth distance, Sn(Mn)-O2, which corresponds to the apical oxygen that is shared with the Sr (La)-O rock salt sublattice. This elongation is related to the atomic rumpling at the rock salt-perovskite interface and is the source of a deformation in the $Sn(Mn)O_6$ octahedra. This distortion, ascribed to the Irrep Γ_1^+, competes with the rotation of the BO_6 octahedra (associated with the Irrep X_2^+) in bilayered RP phases and can suppress the HIF mechanism, as shown by first-principle calculations [19]. The mode decomposition for the crystal structure of the whole $Sr_{3-x}La_xSn_{2-x}Mn_xO_7$ series is reported in the supplementary information (Table S4). The contribution of the modes associated with the Irrep Γ_1^+ is minor in $Sr_3Sn_2O_7$ but its amplitude increases as the La and Mn content increases in the $Sr_{3-x}La_xSn_{2-x}Mn_xO_7$ series. This effect may be related to the suppression of the rotation associated with the Irrep X_2^+ and may explain the inhibition of ferroelectricity at room temperature in samples with $x \geq 0.25$. Besides, some studies on related systems have revealed that the presence of trivalent cations (like La^{3+}) in the rock salt layer seems to favor this atomic rumpling [38]. Our refinements (see Table S5 in the supplementary information) reveal that La occupies both perovskite (A1) and rock-salt (A2) crystallographic sites, but with a slight preference for the rock-salt site, which could be the origin for the enhancement of the rumpling mode. Nonetheless, the structural instabilities caused by the introduction of a formally active JT Mn^{3+} cation cannot be discarded as a plausible mechanism for the destabilization of the polar $A2_1am$

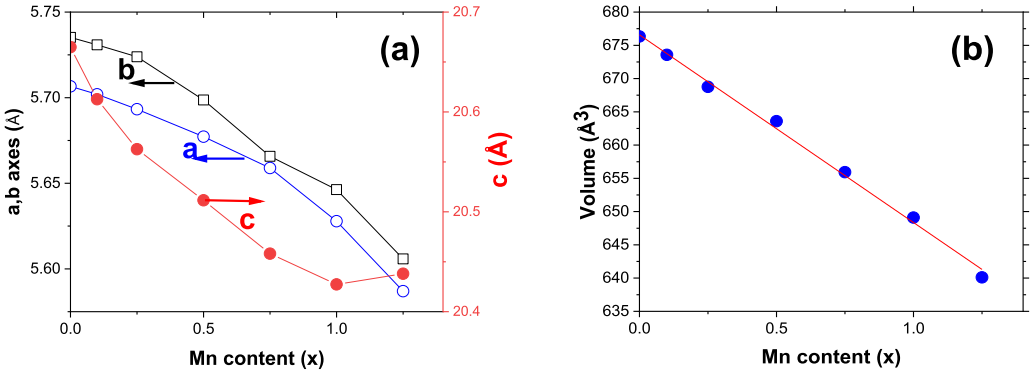

Fig. 2. Refined lattice parameters (a) and unit cell volume (b) for $Sr_{3-x}La_xSn_{2-x}Mn_xO_7$ samples.

structure.

3.2. X-ray absorption spectroscopy at the Mn K- and $L_{2,3}$-edges

Normalized XANES spectra of the $Sr_{3-x}La_xSn_{2-x}Mn_xO_7$ ($0.1 \leq x \leq 1$) series at the Mn K edge are compared to reference compounds for formal Mn^{3+} ($LaMnO_3$) and Mn^{4+} ($CaMnO_3$ and $Ca_3Mn_2O_7$) in Fig. 3(a). The energy position of the absorption edge of Mn^{4+} references is shifted ~4 eV with respect to the Mn^{3+} reference, in agreement with previous experimental observations within the error bar (~ 0.3 eV) [39,40]. The spectral line shape of XANES for $Sr_{3-x}La_xSn_{2-x}Mn_xO_7$ is similar for all compositions, suggesting an equivalent local environment for Mn atoms along the whole series. The energy position of the absorption edges is close to the Mn^{3+} reference in all cases, but shifted about 1 eV towards higher values. Considering the linear dependence of the absorption edge shift and the formal valence, this shift indicates oxidation state values around $Mn^{3.25+}$ for the whole series (see Fig. 3(b)). Given the synthesis conditions, a change in Mn oxidation state is highly unlikely and is not supported by the Mn $L_{2,3}$-edge spectra (see discussion below). However, the threshold energy is not only sensitive to the electronic state of the absorbing atom but also to its local structure, *i.e.*, its first neighbor bonds [40]. In this way, $LaMnO_3$ is a prototypical JT active compound, where Mn^{3+} ions ($3d^4$) induce strong and cooperative distortions of the MnO_6 octahedron due to the presence of an electron in the $3d_z^2$ orbital. When Mn^{3+} is surrounded by non-magnetic cations like Ga^{3+} (with a closed-shell) in the $LaMn_xGa_{1-x}O_3$ series [41], the JT distortion is significantly reduced. This leads to a modification of the local symmetry around Mn sites and a gradual relaxation of the MnO_6 octahedral distortions toward a more regular geometry preserving the Mn^{3+} oxidation state. According to Zhou and Goodenough [42], the incorporation of Ga^{3+} alters both the Mn–O bond lengths and Mn–O–Mn bond angles, thereby reshaping the superexchange pathways. These structural changes promote a static orbital mixing in the remaining Mn^{3+} ions that favor a superposition of $3d_{x-y}^{2\,2}$ and $3d_z^2$ orbitals. As the Ga content increases, the crystal structure evolves toward higher cubic symmetry resulting in an undistorted MnO_6 octahedron. This structural homogenization facilitates isotropic orbital overlap and stabilizes three-dimensional ferromagnetic coupling, replacing the antiferromagnetic order present in the parent compound. In the XAS study of the $LaMn_{1-x}Ga_xO_3$ series, a shift of the Mn K-absorption edges was observed between JT distorted Mn^{3+} ions and the same cations in an undistorted octahedral environment [24,41]. We have used the spectra from that series for comparative purposes and we have observed that the small shift in the XANES threshold energy between $Sr_{3-x}La_xSn_{2-x}Mn_xO_7$ samples and $LaMnO_3$ corresponds very well with the ones between $LaMn_{1-x}Ga_xO_3$ and $LaMnO_3$. This suggests that both Ga^{3+} and Sn^{4+}, two cations with closed *d*-shells, exert the same effect on their neighboring Mn. Fig. 3(b) includes the formal valence evolution with Mn concentration for both $Sr_{3-x}La_xSn_{2-x}Mn_xO_7$ and $LaMn_xGa_{1-x}O_3$ series, based on the edge energy, which indicates a comparable formal valence between the two series for Mn contents below 50 %. The difference is within the error bars and is similar to that found in the two reference compounds of Mn^{4+} in Fig. 3(b), ascribed to the different chemical environment beyond the first coordination shell (3D perovskites and bilayer RP phases). Thus, XANES measurements at the Mn K edge are consistent with the presence of a Mn^{3+} without JT distortion in both $Sr_{3-x}La_xSn_{2-x}Mn_xO_7$ ($0.1 \leq x \leq 1$) and $LaMn_xGa_{1-x}O_3$ ($x \leq 0.5$) series.

Mn $L_{2,3}$-edge XAS data from $Sr_2LaSnMnO_7$ are presented in Fig. 4, together with the spectra of other Mn-oxide compounds with a well-defined Mn valence, such as $La_{1/2}Sr_{1/2}Mn_{1/2}Sn_{1/2}O_3$ (3+) and $Ca_3Mn_2O_7$ (4+). As shown in Fig. 4, the energy position of the $L_{2,3}$ absorption edge is exquisitely sensitive to the valence of an element. The very close match between $Sr_2LaSnMnO_7$ and $La_{1/2}Sr_{1/2}Mn_{1/2}Sn_{1/2}O_3$ $L_{2,3}$-edge energy and line shape, provides further evidence that Mn cations in the $Sr_{3-x}La_xSn_{2-x}Mn_xO_7$ ($0.1 \leq x \leq 1$) series act as Mn^{3+}.

k-weighted EXAFS ($\chi(k)$) signals and their modulus of the Fourier transforms at the Mn K edge for $Sr_{3-x}La_xSn_{2-x}Mn_xO_7$ ($0.1 \leq x \leq 1$) samples are shown in Fig. 5. The Fourier transforms (FTs) were calculated between 3.0 and 12.0 $Å^{-1}$ using a sine window. A main peak corresponding to the first Mn-O coordination shell is noticeable in the radial distribution around 1.4 Å (without phase shift correction). The intensity of this peak decreases and shifts to lower values as the Mn content increases in the samples. Subsequent less intense peaks are also noticeable and mainly correspond to the second, Mn-Sr(La), and third, Mn-O-Sn(Mn), coordination shells. The intensity of these peaks changes

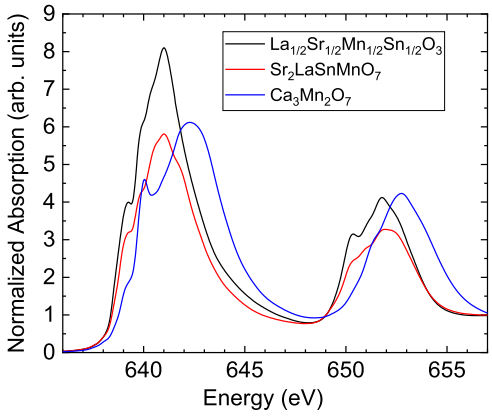

Fig. 4. Mn $L_{2,3}$ edge x-ray absorption spectra of, $Ca_3Mn_2O_7$, $Sr_2LaSnMnO_7$ and $La_{1/2}Sr_{1/2}Mn_{1/2}Sn_{1/2}O_3$ at 300 K.

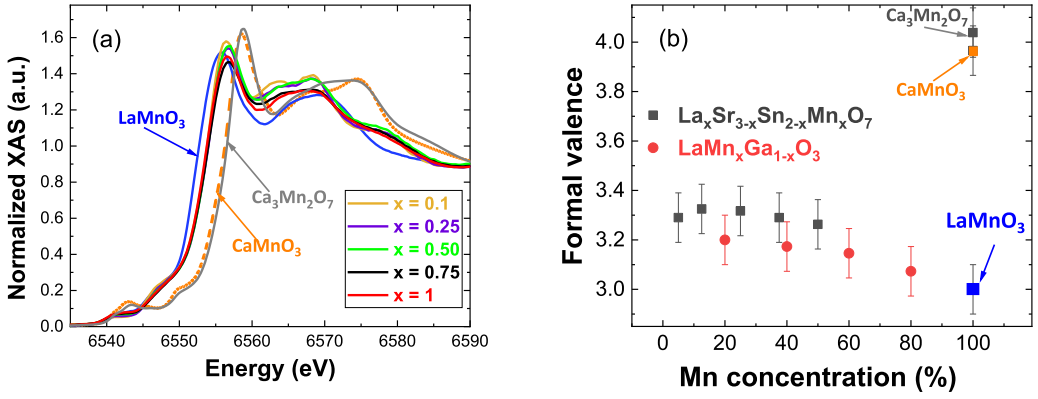

Fig. 3. (a) Normalized XANES spectra for the $Sr_{3-x}La_xSn_{2-x}Mn_xO_7$ ($0.1 \leq x \leq 1$) series and selected references: $LaMnO_3$ (Mn^{3+}), $CaMnO_3$ (Mn^{4+} and 3D) and $Ca_3Mn_2O_7$ (Mn^{4+} and RP phase). (b) Formal valence state inferred from the energy threshold of the XANES for $Sr_{3-x}La_xSn_{2-x}Mn_xO_7$ ($0.1 \leq x \leq 1$) series compared to the $LaMn_xGa_{1-x}O_3$ series from Refs. 24, 40 and 41, as a function of Mn concentration.

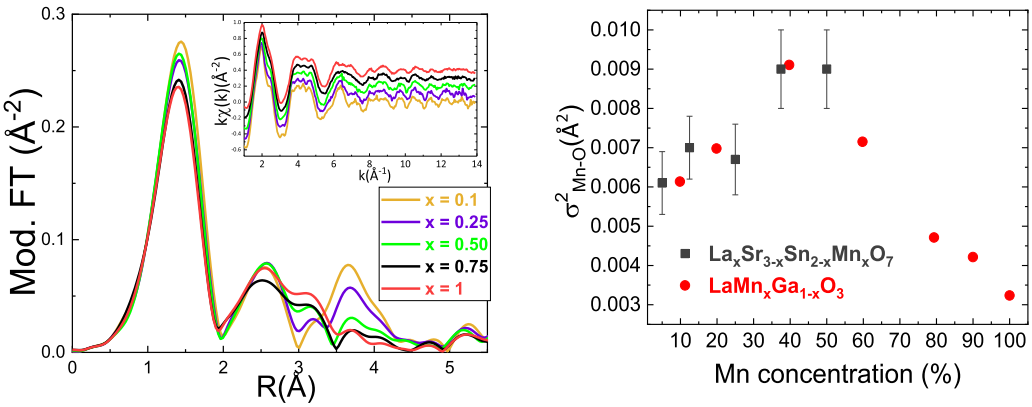

Fig. 5. (a) Fourier transform of the experimental $k\,\chi(k)$ EXAFS signals for selected compositions of the $Sr_{3-x}La_xSn_{2-x}Mn_xO_7$ ($0.1 \leq x \leq 1$) series. Inset: corresponding $k\,\chi(k)$ EXAFS signals at the Mn K edge. (b) Evolution of EXAFS Debye Waller factor of the average Mn-O bond length with Mn concentration for the $Sr_{3-x}La_xSn_{2-x}Mn_xO_7$ ($0.1 \leq x \leq 1$) (black squares) compared to the $LaMn_xGa_{1-x}O_3$ series from ref. [41] (red points).

more intensely along the series due to changes in the chemical composition (Sr/La and Sn/Mn distributions).

The EXAFS analysis was focused on the first coordination shell to discern the presence of JT distortions of the MnO_6 octahedron. Initially, we investigated whether a Mn^{3+} ion with JT distortion was possible (*i.e.,* 4 short Mn-O bonds and 2 large Mn-O distances). The fits were very unreliable featuring several local minima, including in some cases four long and two short Mn-O distances (the opposite of what was expected) and the goodness-of-fits factors (R fits) were very poor (see Fig. S7 for illustration in the supplementary information). This means that a JT Mn^{3+} cation cannot account for the Mn local structure in the $Sr_{3-x}La_xSn_{2-x}Mn_xO_7$ series. Next, we tested two models: (i) a single average Mn-O distance for the six bonds, i.e., an undistorted octahedron, as for non-JT active Mn^{3+}, and (ii) a distorted MnO_6 octahedron with a single elongated bond (hereafter denoted by SEB-octahedron) composed by 5 short Mn-O distances and one long, as observed in the crystallographic refinement (see previous section).

Model (ii) works worse for samples with $x \leq 0.5$, where model (i) with an undistorted octahedron provides adequate fits, as summarized in Table 1. However, for $x \geq 0.75$ model (ii) yields better R-fits factors compared to those obtained with an undistorted octahedron, suggesting a correlation between the enhancement of the rumpling distortion and the Mn content in the samples. Model (i), with a single average Mn-O distance, yields results comparable to those obtained from the crystallographic solution that averages the Sn(Mn)-O environments. According to model (i), Mn-O bond length decreases as the Mn content increases in the series. This agrees with the shift of the peak position of the FT (see Fig. 4) and with the contraction of the unit cell (see Fig. 2). Likewise, there is an increase of the Debye-Waller (σ^2) factors (Fig. 4(b)) that can be ascribed to the increase of the rumpling distortion with increasing x-value, as previously indicated (see previous section). Besides, the values of the σ^2 factors are alike the values obtained for $LaMn_xGa_{1-x}O_3$ for $x \leq 0.5$, with an undistorted MnO_6 octahedra distribution [41].

3.3. Macroscopic magnetic properties

The M(H) loops for $Sr_{3-x}La_xSn_{2-x}Mn_xO_7$ at 5 K show spontaneous magnetization typical of a ferromagnetic component (Fig. 6(a)). As the Mn concentration increases in the series, both the coercivity (H_C) and remanent magnetization (M_r) exhibit a systematic enhancement. The most diluted sample ($x = 0.1$) exhibits negligible H_C and M_r values. At low Mn content ($x = 0.25$–0.5), the magnetic signal is very weak (M_r ranging between 1.2×10^{-3} and 3×10^{-3} μ_B*/f.u.)*, with very small hysteresis (H_C = 5–14 Oe), suggesting a predominantly paramagnetic regime with minimal magnetic coupling. For $x \geq 0.75$, the hysteresis loops become increasingly open, with H (30, 115 and 245 Oe for $x = 0.75$, 1, and 1.25, respectively) and M_r (7.6×10^{-3}, 5.2×10^{-2} and 8×10^{-2} μ_B*/f.u*) rising significantly. This trend implies the development of stronger magnetic interactions, possibly due to the formation of locally correlated regions or magnetic domains. The increasing coercivity suggests that the system becomes more resistant to magnetization reversal, while the enhanced remanence points to a growing ability to retain magnetic alignment after the external field is removed. These observations may reflect a transition from isolated magnetic moments to a more cooperative magnetic state as Mn content increases. However, comparison of the M(H) curves normalized to Mn content reveals that the magnetic moment per Mn atom falls short of the expected value of 4 μ_B for Mn^{3+} cations. (Fig. 6(b)). This behavior is in contrast with the simple perovskite, $La_{1/2}Sr_{1/2}Mn_{1/2}Sn_{1/2}O_3$, which shows a soft ferromagnetic loop with a saturated moment close to 4 μ_B per Mn atom. Magnetization in the $Sr_{3-x}La_xSn_{2-x}Mn_xO_7$ series does not saturate at 50 kOe and reaches values of approximately 2.6–3 μ_B per Mn atom. Samples with $x = 0.5$ and 0.75 exhibit higher magnetization, suggesting they are more easily polarizable. Considering the EXAFS results presented in the previous section, the low Mn-diluted samples, characterized by regular MnO_6 octahedra, appear to be more readily magnetized under an external field (Fig. 6b). As the concentration of magnetic Mn

Table 1
EXAFS-derived parameters for $Sr_{3-x}La_xSn_{2-x}Mn_xO_7$ ($x \leq 1$) at the Mn K-Edge obtained by fitting the k^2-Weighted EXAFS oscillations in R-space corresponding to the 1st coordination shell using either an undistorted MnO_6 octahedron or a SEB MnO_6 octahedron in agreement with the X-ray diffraction study. The amplitude reduction factor, s_0^2, was fixed to 0.75, and the threshold energy (ΔE_0) was fixed to the average value of −4.7 eV to minimize free parameters. The coordination numbers were kept constant (see table) and only, the radial distances and the σ^2 factors were considered as fitting parameters.

Mn-content		Model (i) undistorted MnO_6			Model (ii) SEB-MnO_6			
(x)	(%)	**Mn-O** (Å) × 6	σ^2 (Å^2)	**R fit**	**Mn-O$_{short}$** (Å) × 5	**Mn-O$_{long}$** (Å) × 1	σ^2 (Å^2)	**R fit**
0.1	5	1.96(1)	0.0063(9)	0.006	1.941(7)	2.141(7)	0.003(1)	0.018
0.25	12.5	1.952(5)	0.0073(9)	0.009	1.934(6)	2.134(6)	0.004(1)	0.013
0.5	25	1.942(6)	0.007(1)	0.014	1.930(6)	2.130(6)	0.003(1)	0.013
0.75	37.5	1.935(7)	0.009(1)	0.02	1.918(7)	2.118(7)	0.005(1)	0.016
1	50	1.935(6)	0.009(1)	0.016	1.919(6)	2.119(6)	0.0052(9)	0.014

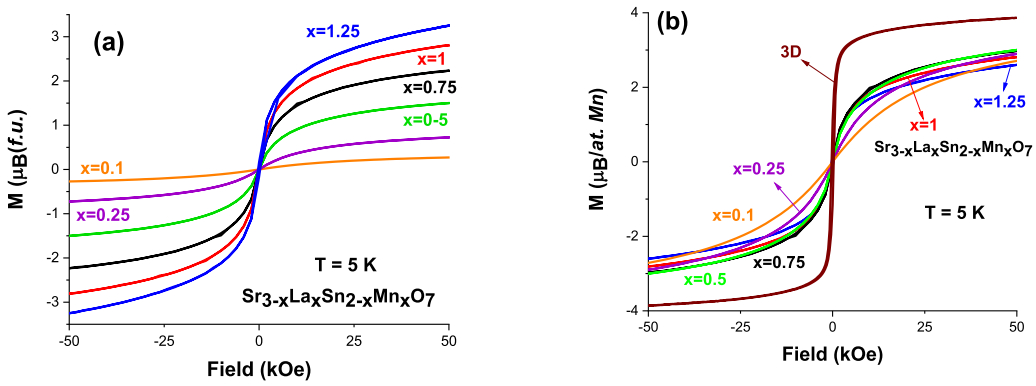

Fig. 6. (a) M(H) measurements for $Sr_{3-x}La_xSn_{2-x}Mn_xO_7$ samples at 5 K. (b) Comparison of the M(H) loops between $La_{1/2}Sr_{1/2}Mn_{1/2}Sn_{1/2}O_3$ (3D) and $Sr_{3-x}La_xSn_{2-x}Mn_xO_7$ samples at 5 K normalized to the Mn content of each sample.

ions in the lattice increases, one would naturally expect a corresponding rise in the number of magnetic interactions. This should, in principle, favor the emergence of long-range ferromagnetic order, leading the system closer to the theoretical saturation value of 4 μ_B per Mn atom. Surprisingly, this trend is not observed. On the contrary, the magnetic moment per Mn atom measured at 5 T either plateaus or even decreases for compositions with $x > 0.75$. When this unexpected behavior is examined alongside the structural analysis presented earlier, a clear correlation emerges: the samples with higher Mn content also exhibit a pronounced increase in rumpling distortion. This structural distortion may likely disrupt the abovementioned *3d* orbital mixing, thereby hindering efficient spin alignment and suppressing the expected enhancement in magnetization.

Fig. 7 shows the magnetization vs. temperature curves, M(T), for $Sr_{3-x}La_xSn_{2-x}Mn_xO_7$ samples compared to $La_{1/2}Sr_{1/2}Mn_{1/2}Sn_{1/2}O_3$, which exhibits a long-range magnetic order with minor zero-field-cooled (ZFC) and field-cooled (FC) irreversibility at 1 kOe [27]. No anomalies are observed in the M(T) curves for $x \leq 0.5$ between 5 K and room temperature, in agreement with a paramagnetic ground state. Notably, there is a significant increase in magnetization at low temperatures. Otherwise, M(T) curves of $x \geq 0.75$ samples exhibit magnetic irreversibility between ZFC and FC measurements and the ZFC curve shows a peak, absent in the FC curve that continuously increases with decreasing temperature. The irreversibility region (separation between the two branches) increases as the Mn content does. This kind of measurement was carried out under different external fields for $Sr_2LaSnMnO_7$ (see Fig. S8 in the supplementary section). The peak temperature in the ZFC curve decreases with increasing the strength of the magnetic field. Accordingly, the differences between the ZFC and FC curves are more pronounced at low external magnetic field strengths (100 Oe), but remarkably vanish at high external magnetic field strengths (10 kOe), indicating that the external field helps to align the spins, reducing disorder and irreversibility in these samples. Overall, the observed behavior suggests either the presence of a magnetic system with disorder and frustration, possibly in a magnetic glassy phase [43], or the contribution of domain effects in an ordered system [44].

To distinguish between these possibilities, neutron powder diffraction patterns for $Sr_2LaSnMnO_7$ have been collected over a temperature range of 2–150 K. Fig. 8 compares the measured patterns below and well above the irreversibility observed in Fig. 7 (see also Fig. S8 in the supplementary section). The pattern recorded at 2 K shows neither additional diffraction peaks nor intensity changes in the allowed reflections, indicating the absence of long-range magnetic order in this compound. The only significant difference between the two measurements is the strong increase in diffuse scattering at low angles. This feature has been ascribed to strong short-range ferromagnetic correlations in related 3D manganites [45].

Our results suggest that structural disorder and competitive magnetic interactions have led to the emergence of a glassy magnetic state in $Sr_{3-x}La_xSn_{2-x}Mn_xO_7$ samples at low temperature. To verify this, we conducted AC magnetic susceptibility measurements of $Sr_2LaSnMnO_7$ at different frequencies (Fig. 9). A peak in the real component is observed at 14.8 K (900 Hz), which shifts slightly to lower temperatures while increasing intensity as the frequency of the magnetic field decreases. This change in intensity arises because the spins fail to follow the high-frequency magnetic field efficiently, leading to a diminished response [43]. In contrast, the imaginary component exhibits a broad maximum at lower temperatures compared to the real component. In this case, the

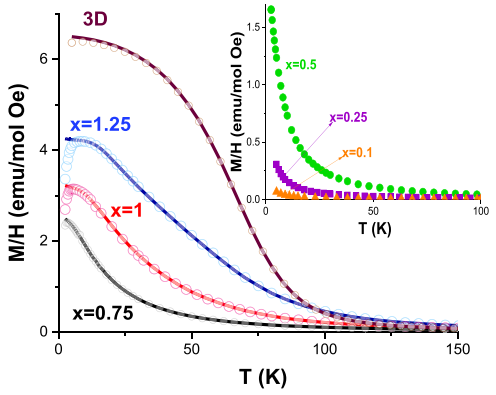

Fig. 7. Magnetization vs. Temperature for $Sr_{3-x}La_xSn_{2-x}Mn_xO_7$ samples (x is given for each curve) and the 3D perovskite $La_{1/2}Sr_{1/2}Mn_{1/2}Sn_{1/2}O_3$. The measurements were performed at 1 kOe in ZFC (symbols) and FC (lines) conditions. Inset: M(T) curves for $x \leq 0.5$ samples.

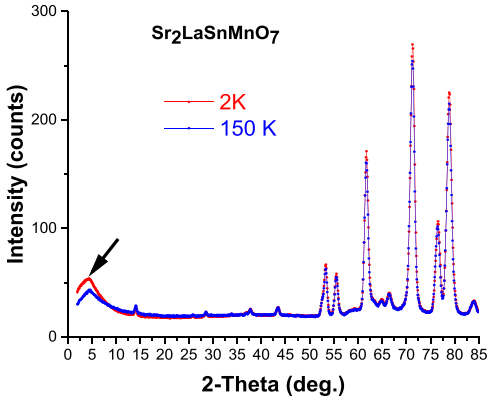

Fig. 8. Comparison of the neutron powder diffraction patterns for $Sr_2LaSnMnO_7$ collected at 2 and 150 K. The arrow indicates the enhancement of low angle diffuse scattering at low temperatures.

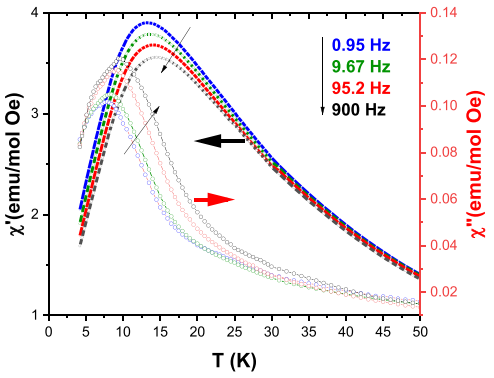

Fig. 9. The in-phase and out-of-phase ac magnetic susceptibility vs. temperature curves for the $Sr_2LaSnMnO_7$ sample measured at the indicated frequencies, and using an alternating field of 2 Oe.

peak intensity increases at higher frequencies due to greater energy dissipation (internal friction) at higher frequencies. The nature of the magnetic freezing was investigated through both the Mydosh parameter (δ) and dynamic scaling analysis. The frequency dependence of the freezing temperature is defined as: $\delta = \Delta T_f/[T_f \times \Delta(\log_{10} f)]$ where ΔT_f is the change in freezing temperature between two frequencies, T_f is the average freezing temperature and $\Delta(\log_{10} f)$ is the change in the logarithm of the frequency [43]. The calculated value of δ for Fig. 8 is approximately 0.04, which exceeds the typical range for canonical spin-glasses (0.005–0.02) but remains well below the threshold for superparamagnetic behavior (>0.1). This intermediate value is consistent with a cluster-glass state, where magnetic freezing involves correlated spin clusters rather than isolated spins. Such behavior suggests the presence of competing magnetic interactions and short-range order without long-range magnetic coherence. To further probe the dynamics, the critical slowing down was analyzed using the power-law relation:

$$\tau = \tau_0 \left(\frac{T_f - T_g}{T_g}\right)^{-z\nu}$$

Where τ is the relaxation time of magnetic clusters at freezing temperature T_f at a given frequency ($\tau = 1/2\pi f$), τ_0 is a microscopic characteristic time (fastest possible magnetic relaxation time), T_g is the glass transition temperature (where dynamics freeze completely) and $-z\nu$ is a dynamic critical exponent. The fit (shown in the Fig. S14 of the supplementary material) yielded $T_g = 9.8$ K, $z\nu = 15.7$ and $\tau_0 = 4.2 \times 10^{-9}$ sec. A $z\nu$ value well above the canonical range (typically 4–12) and τ_0 in the range of nanoseconds reinforces the interpretation of a slow, collective freezing process consistent with cluster-glass dynamics [43,46]. In cluster-glass systems, fast relaxation times on the order of nanoseconds reflect the rapid, local dynamics of small magnetic clusters, which can fluctuate independently due to low internal energy barriers. However, as the system approaches the freezing temperature, interactions between clusters become increasingly significant, leading to cooperative behavior and a dramatic slowdown in the overall magnetic response—this is captured by a high dynamic exponent ($z\nu$), indicating a critical slowing down. So, while individual clusters remain agile, their collective dynamics become sluggish near the glass transition, reconciling fast microscopic motion with slow macroscopic evolution.

As the concentration of Mn^{3+} increases, magnetic interactions strengthen, leading to short-range magnetic correlations. However, the percolation threshold is not reached, preventing the formation of long-range magnetic order—unlike in 3D perovskites. This suggests that the rock salt layer separating the bilayers of $Sn(Mn)O_6$ octahedra plays a crucial role in suppressing long-range ferromagnetic order, as observed in related compounds [20].

The temperature dependence for the inverse dc susceptibility is reported in the supplementary section. All samples show a linear behavior at high temperature and deviate from a Curie-Weiss law at low temperature (see Fig. S9-S13). The magnetic data extracted from the linear fit are also detailed in Table 2. The Curie constant increases as the Mn content does and all compounds present FM correlations (positive Weiss constants) in contrast to the expected Mn^{3+}-O-Mn^{3+} superexchange interactions according to the Goodenough-Kanamori rules [47,48], but in agreement with the ferromagnetic ground state found in related 3D perovskites [24–27]. The ρ_{eff} values reasonably agree with the spin-only contribution (ρ_{the}) for Mn^{3+} cations in the diluted samples ($x \leq 0.25$), but deviations occur as co-doping increases ($\rho_{eff} > \rho_{the}$). The increase in ρ_{eff} comes from the enhancement of magnetic correlations as the Mn concentration increases, as XAS measurements have discarded the presence of any Mn^{2+} contribution. The observed increase in ρ_{eff} is not unusually large, but it is meaningful. In cluster-glass systems, even well above the freezing temperature, short-range spin correlations can lead to the formation of dynamic clusters. These clusters behave as collective magnetic entities, slightly enhancing the magnetic response compared to isolated ions. In the present system with high-spin Mn^{3+} (d^4), the absence of a JT distortion due to structural constraints allows the e_g electron to dynamically fluctuate between degenerate orbitals. This orbital fluctuation introduces a form of dynamic degeneracy that can couple with spin degrees of freedom, subtly enhancing magnetic interactions. As a result, the effective magnetic moment may slightly exceed the spin-only value.

4. Conclusions

We report on the structural and magnetic properties of the newly synthesized $Sr_{3-x}La_xSn_{2-x}Mn_xO_7$ series, whose behavior is strongly influenced by the Mn and La concentrations. At low doping levels ($x \leq 0.1$), the compounds crystallize in a non-centrosymmetric orthorhombic structure with space group $A2_1am$ and thus are expected to exhibit ferroelectricity. As the concentration increases ($x \geq 0.25$), a structural transition occurs toward the centrosymmetric space group *Amam* at room temperature. This transition is attributed to the loss of specific rotational modes within the crystal lattice. Although Mn^{3+} is typically JT active, XAS confirms that the distortion is effectively suppressed in this series due to the influence of neighboring Sn^{4+} ions. This stabilization of undistorted MnO_6 octahedra promotes isotropic orbital overlap, favoring three-dimensional ferromagnetic coupling. Additionally, increasing Mn content leads to a reduction in Mn–O bond lengths and a concurrent rise in atomic rumpling, particularly at the interfaces between perovskite and rock-salt layers, resulting in an enhanced structural disorder.

Regarding the magnetic properties, all samples exhibit ferromagnetic correlations at low temperatures, but long-range magnetic ordering is not achieved. Instead, they develop magnetic phases consistent with cluster-glass behavior. This suggests that the magnetic percolation threshold in this layered system is well above 50 % Mn content, in contrast to similar 3D perovskites. Two key factors account for this behavior. First, the presence of non-magnetic rock-salt layers disrupts magnetic coherence between the perovskite bilayers, thereby hindering the development of long-range order. Second, the atomic rumpling,

Table 2
Curie constant (C), Weiss constant (θ) and experimental effective paramagnetic moments (ρ_{eff}) obtained from the fit to a Curie-Weiss law above 150–200 K. Theoretical effective paramagnetic moments (ρ_{theo}) have been calculated from experimental values for spin-only contribution of high-spin Mn^{3+}.

Sample	C (emu/K mol)	θ (K)	ρ_{eff} (μ_B/*fu*)	ρ_{theo} (μ_B/*fu*)
x = 0.1	0.27	31.1	1.47	1.55
x = 0.25	0.84	47.6	2.59	2.45
x = 0.5	1.825	84.4	3.82	3.46
x = 0.75	2.95	108.8	4.85	4.24
x = 1	4.15	121.8	5.76	4.90
x = 1.25	5.24	134.9	6.47	5.47

which is enhanced in samples with high Mn content, weakens the strength of the ferromagnetic interactions. Overall, these results provide experimental evidence that structural disorder and rumpling distortions are critical factors governing the magnetic behavior of these layered materials, with important implications for the design of magnetoelectric multiferroic materials.

Declaration of Competing Interest

The authors declare that they have no known competing financial interests or personal relationships that could have appeared to influence the work reported in this paper.

Acknowledgements

For financial support, we thank grants PID2021–124734OB-C21 and -C22 together with grant CEX2023–001286-S funded by MICIU/AEI/10.13039/501100011033 and, as appropriate, by "ERDF A way of making Europe" and Diputación General de Aragón (projects E11–23R and E12–23R). D. G. acknowledges financial support from the Gobierno de Aragón through a doctoral fellowship. Authors would also like to acknowledge Servicio General de Apoyo a la Investigación from Universidad de Zaragoza. Granted beam time at ILL, via Spanish Initiatives on Neutron Scattering (SpINS), is also appreciated (Experiment CRG-2990; doi: 10.5291/ILL-DATA.CRG-2990). Beam time allocation at ALBA (proposal codes 2023027292 and 20250330019) and ESRF (exp blc15406) synchrotrons are also acknowledged.

Appendix A. Supporting information

Supplementary data associated with this article can be found in the online version at doi:10.1016/j.jallcom.2025.185048.

References

[1] M. Kumar, S. Shankar, A. Kumar, A. Anshul, M. Jayasimhadri, O.P. Thakur, Progress in multiferroic and magnetoelectric materials: applications, opportunities and challenges, J. Mater. Sci Mater. Electron 31 (2020) 19487–19510, https://doi.org/10.1007/s10854-020-04574-2.

[2] B. Jana, K. Ghosh, K. Rudrapal, P. Gaur, P.K. Shihabudeen, A.R. Chaudhuri, Recent progress in flexible multiferroics, Front. Phys. 9 (2022) 822005, https://doi.org/10.3389/fphy.2021.822005.

[3] K.F. Wang, J.-M. Liu, Z.F. Ren, Multiferroicity: the coupling between magnetic and polarization orders, Adv. Phys. 58 (2009) 321–448, https://doi.org/10.1080/00018730902920554.

[4] N.A. Hill, Why are there so few magnetic ferroelectrics? J. Phys. Chem. B 104 (2000) 6694–6709, https://doi.org/10.1021/jp000114x.

[5] A. Marthinsen, C. Faber, U. Aschauer, N.A. Spaldin, S.M. Selbach, Coupling and competition between ferroelectricity, magnetism, strain, and oxygen vacancies in AMnO3 perovskites, MRS Comm. 6 (2016) 182–191, https://doi.org/10.1557/mrc.2016.30.

[6] N.A. Benedek, C.J. Fennie, Hybrid improper ferroelectricity: a mechanism for controllable polarization-magnetization coupling, Phys. Rev. Lett. 106 (2011) 107204, https://doi.org/10.1103/PhysRevLett.106.107204.

[7] I. Etxeberria, J.M. Pérez-Mato, P. Boullay, The role of trilinear couplings in the phase transitions of aurivillius compounds, Ferroelectrics 401 (2010) 17–23, https://doi.org/10.1080/00150191003670325.

[8] N.A. Benedek, J.M. Rondinelli, H. Djani, P. Ghosez, P. Lightfoot, Understanding ferroelectricity in layered perovskites: new ideas and insights from theory and experiments, Dalt. Trans. 44 (2015) 10543–10558, https://doi.org/10.1039/C5DT00010F.

[9] N.A. Benedek, M.A. Hayward, Hybrid improper ferroelectricity: a theoretical, computational, and synthetic perspective, Ann. Rev. Mater. Res. 52 (2020) 331–355, https://doi.org/10.1146/annurev-matsci-080819-010313.

[10] M.J. Pitcher, P. Mandal, M.S. Dyer, J. Alaria, P. Borisov, H. Niu, J.B. Claridge, M. J. Rosseinsky, Magnetic materials. Tilt engineering of spontaneous polarization and magnetization above 300 K in a bulk layered perovskite, Science 347 (2015) 420–424, https://doi.org/10.1126/science.1262118.

[11] Y. Wang, F.-T. Huang, X. Luo, B. Gao, S.-W. Cheong, The first room-temperature ferroelectric Sn insulator and its polarization switching kinetics, Adv. Mater. 29 (2017) 1601288, https://doi.org/10.1002/adma.201601288.

[12] J.J. Lu, X.Q. Liu, X. Ma, M.S. Fu, A. Yuan, Y.J. Wu, X.M. Chen, Crystal structures, dielectric properties, and phase transition in hybrid improper ferroelectric $Sr_3Sn_2O_7$-based ceramics, J. Appl. Phys. 125 (2019) 044101, https://doi.org/10.1063/1.5051190.

[13] S. Yoshida, H. Akamatsu, R. Tsuji, O. Hernandez, H. Padmanabhan, A.S. Gupta, A. S. Gibbs, K. Mibu, S. Murai, J.M. Rondinelli, V. Gopalan, K. Tanaka, K. Fujita, Hybrid Improper Ferroelectricity in $(Sr,Ca)_3Sn_2O_7$ and Beyond: Universal Relationship between Ferroelectric Transition Temperature and Tolerance Factor in n = 2 Ruddlesden−Popper Phases, J. Am. Chem. Soc. 140 (2018) 15690, https://pubs.acs.org/doi/10.1021/jacs.8b07998.

[14] K.-E. Hasin, N. Pokrel, E.A. Nowadnick, Piezoelectricity in n = 2 Ruddlesden–Popper Ferroelectric Oxides, Chem. Mat. 36 (2024) 7552, https://doi.org/10.1021/acs.chemmater.4c01534.

[15] X. Sun, X. Yang, C. Xu, X. Gan, W. Zhang, Z. Gao, H.L. Cai, X.S. Wu, Effects of Ba doping on the phase transition of Sr3Sn2O7, Chem. Phys. Lett. 728 (2019) 74–79, https://doi.org/10.1016/j.cplett.2019.04.083.

[16] X. Sun, Z. Tang, X. Yang, Z. Gao, Y. Wu, J. Jiang, Z. Zhang, S. Jiao, D. Li, H.-L. Cai, X.S. Wu, Structural evolution and phase transition of $Sr_3Sn_2O_7$ doped with Ca, Chem. Phys. Lett. 766 (2021) 138319, https://doi.org/10.1016/j.cplett.2021.138319.

[17] V.M. Goldschmidt, Die Gesetze der Krystallochemie, Die Nat. 14 (1926) 477–485, https://doi.org/10.1007/bf01507527.

[18] J. Blasco, D. Gracia, S. Lafuerza, V. Cuartero, G. Subías, Effects of doping with magnetic cations on the hybrid improper ferroelectricity in $Sr_3Sn_2O_7$, J. Alloy. Comp. 1005 (2024) 176148, https://doi.org/10.1016/j.jallcom.2024.176148.

[19] Y. Zhang, J. Wang, P. Ghosez, Unraveling the suppression of oxygen octahedral rotations in $A_3B_2O_7$ ruddlesden-popper compounds: engineering multiferroicity and beyond, Phys. Rev. Lett. 125 (2020) 15761, https://doi.org/10.1103/PhysRevLett.125.157601.

[20] J. Blasco, V. Cuartero, S. Lafuerza, D. Gracia, J.A. Rodríguez-Velamazán, I. Puente-Orench, G. Subías, Exploring the magnetic percolation threshold in the improper ferroelectric Sr3Sn2O7 upon Cr and Fe-doping, Mat. Res. Bull. 187 (2025) 113385, https://doi.org/10.1016/j.materresbull.2025.113385.

[21] A.J. Millis, B.I. Shraiman, R. Müller, Dynamic jahn-teller effect and colossal magnetoresistance in La1-xSrxMnO3, Phys. Rev. Lett. 77 (1996) 175–178, https://doi.org/10.1103/PhysRevLett.77.175.

[22] K. Rościszewski, A.M. Oleś, Spin-orbital order in LaMnO3: d−p model study, Phys. Rev. B 99 (2019) 155108, https://doi.org/10.1103/PhysRevB.99.155108.

[23] C. Ritter, M.R. Ibarra, J.M. de Teresa, P.A. Algarabel, C. Marquina, J. Blasco, J. García, S. Oseroff, S.-W. Cheong, Influence of oxygen content on the structural, magnetotransport, and magnetic properties of LaMnO3+δ, Phys. Rev. B 56 (1997) 8902–8911, https://doi.org/10.1103/PhysRevB.56.8902.

[24] M.C. Sánchez, G. Subías, J. García, J. Blasco, Stability of the tetragonal $Mn^{3+}O_6$ distortions in the $LaMn_{1-x}Ga_xO_3$ series by x-ray absorption spectroscopy, Phys. Rev. B 69 (2004) 184415, https://doi.org/10.1103/PhysRevB.69.184415.

[25] J.B. Goodenough, R.I. Dass, J. Zhou, Spin-glass to ferromagnet transition in $LaMn_{1-x}Sc_xO_3$, Sol. State Sci. 4 (2002) 297, https://doi.org/10.1016/S1293-2558(01)01255-9.

[26] J. Blasco, J. García, J. Campo, M.C. Sánchez, G. Subías, Neutron diffraction study and magnetic properties of $LaMn_{1-x}Ga_xO_3$, Phys. Rev. B 66 (2002) 174431, https://doi.org/10.1103/PhysRevB.66.174431.

[27] T. Yang, T. Perkisas, J. Hadermann, M. Croft, A. Ignatov, G. Van Tendeloo, M. Greenblatt, Synthesis and Structure Determination of Ferromagnetic Semiconductors LaAMnSnO6 (A = Sr Ba), J. Mater. Chem. 21 (2011) 199–205, https://doi.org/10.1039/C0JM02614J.

[28] J. Rodríguez-Carvajal, Recent advances in magnetic structure determination by neutron powder diffraction, Phys. B 192 (1993) 55–69, https://doi.org/10.1016/0921-4526(93)90108-I.

[29] A. Barla, J. Nicolas, D. Cocco, S.M. Valvidares, J. Herrero-Martín, P. Gargiani, J. Moldes, C. Ruget, E. Pellegrin, S. Ferrer, Design and performance of BOREAS, the beamline for resonant X-ray absorption and scattering experiments at the ALBA synchrotron light source, J. Synchrotron Rad. 23 (2016) 1507–1517, https://doi.org/10.1107/S1600577516013461.

[30] O. Mathon, A. Beteva, J. Borrel, D. Bugnazet, S. Gatla, R. Hino, I. Kantor, T. Mairs, M. Munoz, S. Pasternak, F. Perrin, S. Pascarelli, The time-resolved and extreme conditions XAS (TEXAS) facility at the European Synchrotron Radiation Facility: the general-purpose EXAFS bending-magnet beamline BM23, J. Synchrotron Radiat. 22 (2015) 1548, https://doi.org/10.1107/S1600577515017786.

[31] B. Ravel, M. Newville, ATHENA, ARTEMIS, HEPHAESTUS: data analysis for X-ray absorption spectroscopy using IFEFFIT, J. Synchrotron Radiat. 12 (2005) 537, https://doi.org/10.1107/S0909049505012719.

[32] Z. Xiao, T. Xiao, S. Wang, S. Huang, B. Wei, W. Liu, the novel electrical properties in quasi-2D hybrid improper ferroelectric Sr3Sn2O7 ceramic and the structural modulation, J. Am. Ceram. Soc. 107 (2024) 334–343, https://doi.org/10.1111/jace.19457.

[33] J.M. Pérez-Mato, D. Orobengoa, M.I. Aroyo, Mode crystallography of distorted structures, Acta Cryst. A 66 (2010) 558–590, https://doi.org/10.1107/S0108767310016247.

[34] B.J. Campbell, H.T. Stokes, D.E. Tanner, D.M. Hatch, ISODISPLACE: a web-based tool for exploring structural distortions, J. Appl. Crystallogr 39 (2006) 607, https://doi.org/10.1107/S0021889806014075.

[35] A.M. Glazer, Simple ways of determining perovskite structures, Acta Cryst. A 31 (1975) 756, https://doi.org/10.1107/S0567739475001635.

[36] R.D. Shannon, Revised effective ionic radii and systematic studies of interatomie distances in halides and chaleogenides, Acta Cryst. A23 (1976) 751–767, https://doi.org/10.1107/S0567739476001551.

[37] I.D. Brown, R.D. Shannon, Empirical bond-strength—bond-length curves for oxides, Acta Cryst. A 29 (1973) 266–282, https://doi.org/10.1107/S0567739473000689.

[38] W. Yi, T. Kawasaki, Y. Zhang, H. Akamatsu, R. Ota, S. Torii, K. Fujita, La2SrSc2O7: a-Site Cation disorder induces ferroelectricity in ruddlesden-popper layered perovskite oxide, J. Am. Chem. Soc. 146 (2024) 4570, https://doi.org/10.1021/jacs.3c11546.

[39] G. Subias, J. García, M.G. Proietti, J. Blasco, X-ray-absorption near-edge spectroscopy and circular magnetic x-ray dichroism at the Mn K edge of magnetoresistive manganites, Phys. Rev. B 56 (1997) 8183, https://doi.org/10.1103/PhysRevB.56.8183.

[40] J. García, G. Subías, V. Cuartero, J. Herrero-Martín, On the correlation between the X-ray absorption chemical shift and the formal valence state in mixed-valence manganites, J. Synchrotron Rad. 17 (2010) 386–392, https://doi.org/10.1107/S0909049510010277.

[41] M.C. Sánchez, J. García, G. Subías, J. Blasco, Lack of Jahn-Teller distortion in highly diluted LaMn1-xGaxO3 (x>0.6), Phys. Rev. B 73 (2006) 094416, https://doi.org/10.1103/PhysRevB.73.094416.

[42] J.-S. Zhou, J.B. Goodenough, Orbital mixing and ferromagnetism in LaMn1−xGaxO3, Phys. Rev. B 77 (2008) 172409, https://doi.org/10.1103/PhysRevB.77.172409.

[43] J.A. Mydosh, Spin glasses: redux: an updated experimental/materials survey, Rep. Prog. Phys. 78 (2015) 052501, https://doi.org/10.1088/0034-4885/78/5/052501.

[44] E. Sadrollahi, F.J. Litterst, L. Prodan, V. Tsurkan, A. Loidl, Magnetism of $CuCr_2X_4$ (X=S and Se) spinels studied with muon spin rotation and relaxation, Phys. Rev. B 110 (2024) 054439, https://doi.org/10.1103/PhysRevB.110.054439.

[45] J.M. De Teresa, M.R. Ibarra, P.A. Algarabel, C. Ritter, C. Marquina, J. Blasco, J. García, A. del Moral, Z. Arnold, Evidence for magnetic polarons in the magnetoresistive perovskites, Nature 386 (1997) 256–259, https://doi.org/10.1038/386256a0.

[46] M. Roy-Chowdhury, M.S. Seehra, S. Thota, Optimized analysis of the AC magnetic susceptibility data in several spin-glass systems using the Vogel–Fulcher and Power laws, AIP Adv. 13 (2023) 115020, https://doi.org/10.1063/5.0169800.

[47] J.B. Goodenough, An Interpretation of the Magnetic Properties of the Perovskite Type Mixed Crystals $La_{1-x}Sr_xCoO_{3+\lambda}$, J. Phys. Chem. Solids 6 (1958) 287–297, https://doi.org/10.1016/0022-3697(58)90107-0.

[48] J. Kanamori, Superexchange interaction and symmetry properties of electron orbitals, J. Phys. Chem. Solids 10 (1959) 87, https://doi.org/10.1016/0022-3697(59)90061-7.